Chiral modes at exceptional points in exciton-polariton quantum fluids: Supplemental Material

I. SAMPLE AND EXPERIMENTAL SETUP

The semiconductor sample used in the experiment is a GaAs/AlGaAs microcavity containing 12 quantum wells ($\sim$ 7 nm wide) sandwiched between distributed Bragg reflector mirrors [1]. The quantum wells are located at the antinodes of the photon mode. The sample was mounted on a cold finger in a continuous flow microscopy cryostat and cooled down to $\sim$ 4 K. The exciton resonance is around 1.61 eV at 4 K. The laser is modulated by an Acoustic Optical Modulator (AOM) with the repetition rate of 10 KHz and duty cycle of 5% to reduce sample heating.

Our experimental setup is similar to that used in [2]. The exciton-polariton condensate was formed by illuminating the sample by a quasi-continuous non-resonant linearly polarised pump beam derived from a CW Ti:sapphire laser operating at 730 nm. The pump was structured via a Digital Micromirror Device (DMD) and re-imaged onto the sample at normal incidence through a microscope objective.

Due to the continuous decay of the exciton polaritons in the continuous replenished condensed state, coherent photons escape the cavity as a photoluminescence signal and carry all the information about the spatial, momentum, and phase structure of the condensed exciton polaritons [3]. The photoluminescence was then collected via a free space microscope and analysed with a combination of real space and dispersion imaging techniques.

A Michelson interferometer (Fig. S1) with an arm length 1 m was used to investigate the phase structure [4]. The reference beam was created by selecting an area where the phase is nearly constant and expanding the beam in the reference arm by 15 times using the technique similar to that in Ref. [5].

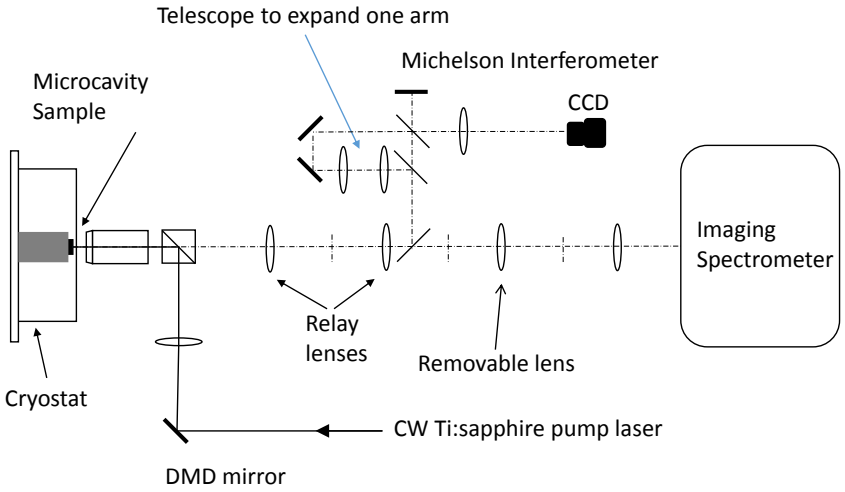

FIG. S1: Schematic of the experimental apparatus demonstrating the main components of the setup: cryostat housing the GaAs/AlGaAs microcavity sample mounted on a cold finger and kept at $\sim$ 4 K, the DMD used to shape the optical excitation, the microscope objective used to collect the photoluminescence, the real and momentum space imaging components and a Michelson interferometer with a telescoping arm (see text).

II. CONDENSATION IN THE RING RESONATOR

Condensation is achieved at a pump power of $P_{th} \sim 12$ mW. Typical images of the lower-polariton (LP) dispersion below the condensation threshold are shown in Fig. S2 for various detunings $\Delta = -3.8$ meV, -3.75 meV, -3.6 meV, -3.4 meV, and -3.2 meV. The variation of detuning is achieved by changing the position of the pump on the sample, and is possible due to a relatively large wedge (length gradient) in the fabricated microcavity [1]. Above the condensation threshold, several ground and excited states of the condensate corresponding to the different spatial modes are clearly resolved, as shown in Fig. S3. The energy spacings between the two dipole states and other energy eigenstates are ~ 0.1 meV, which is two or three times larger than the energy difference between the two dipole modes.

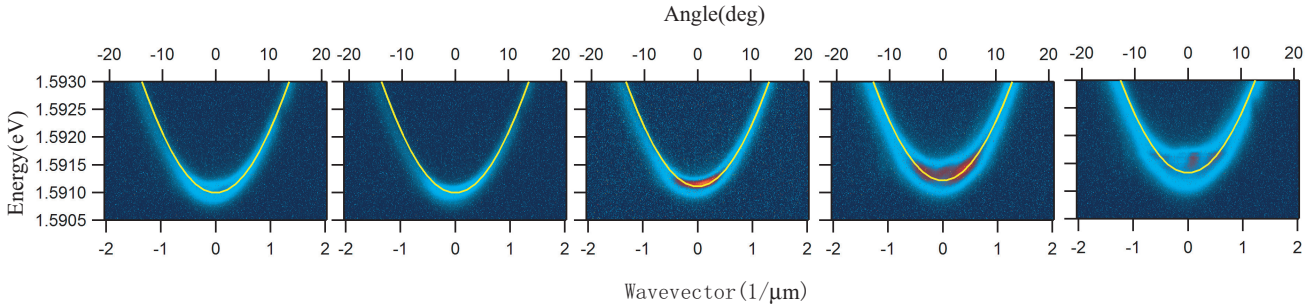

FIG. S2: The lower polariton dispersion at low excitation power far below the polariton condensation threshold at different values of the exciton-photon detuning. The detuning values, from the left to the right panel are: -3.8 meV, -3.75 meV, -3.6 meV, -3.4 meV and -3.2 meV. The white solid line is the fitted lower polariton dispersion curve.

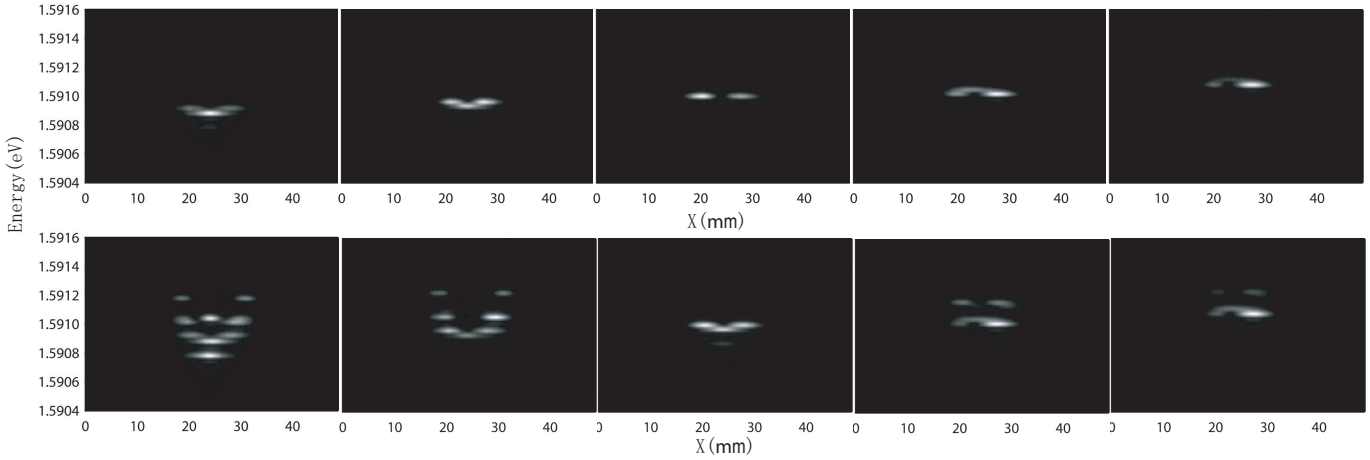

FIG. S3: The energy vs real space imaging above condensation threshold $P/P_{th} \approx 1.5$ for the values of detuning (from the left to the right panels): -3.8 meV, -3.75 meV, -3.6 meV, -3.4 meV, and -3.2 meV. The right half ring width is $w_1 = 1.0\mu$m (top panels) and $w_2 = 1.2\mu$m (bottom panels).

III. EXTRACTING REAL AND IMAGINARY PARTS OF THE EIGENVALUES IN EXPERIMENT

To explore the vicinity of an exceptional point, we change the detuning and width of the right half of the ring resonator (Δ, w) and record the peak position and widths of the spectral lines shown in Fig. S3. These correspond to the real and imaginary parts of the eigenvalues corresponding to the two dipole eigenmodes in the ring resonator, respectively. In order to extract the peak positions and widths, we plot the profiles for the spectral lines along the horizontal direction or vertical direction, depending on the orientation of the dipole mode, as shown in Fig. S4. Because the two dipole modes have orthogonal orientation of the nodal lines, this ensures that we select two independent modes respectively. We note that at some values of the parameters (Δ, w), where the hybridisation

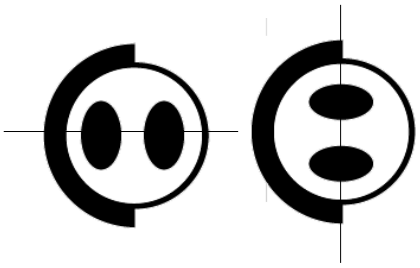

FIG. S4: (a) Schematics for the directions of the real-space energy measurement performed to extract the spectral line profiles in Fig. S5. Shown is the pump-induced resonator and the two dipole modes.

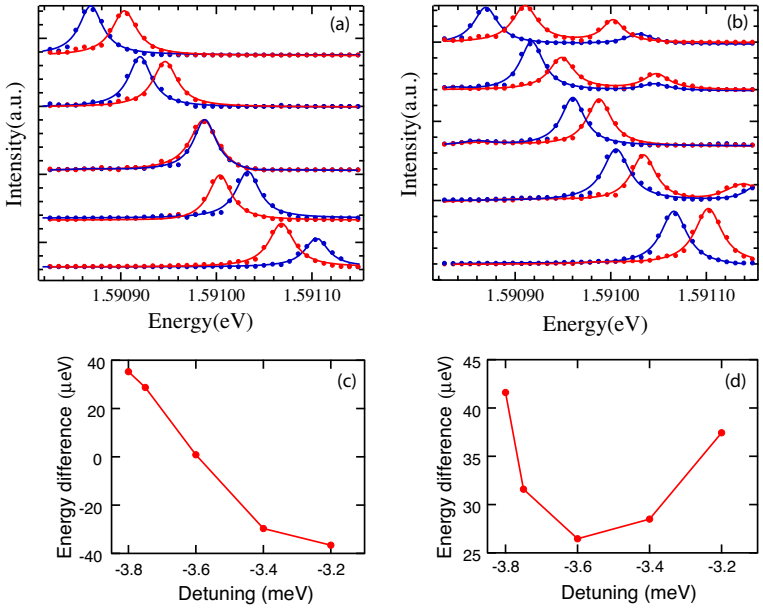

FIG. S5: Spectral line profiles measured for the two dipole modes at (a) $w = 1.0$ μm and (b) $w = 1.2$ μm at different values of detuning Δ, and the corresponding difference in peak positions for the case of (c) crossing and (d) anti-crossing of the energy levels in Fig. 2 of the main text.

between two dipole modes occurs and their spatial mode profiles resemble each other, the line profiles of the modes overlap but can still be distinguishable.

Figures S5(a,b) show the line profiles for these two dipole modes plotted for different values of the detuning Δ and width of the right half ring w corresponding to Fig. 2 in the main text, i.e. when Δ increases from -3.8 meV to -3.2 meV and w is equal to 1.0 and 1.2 μm, respectively. These line profiles are fitted by Lorentzian functions, which allow us to extract the energy peak position and the linewidth corresponding to the two dipole modes. The energy peak positions ordered according to their values and plotted as a function of detuning clearly show the crossing or anti-crossing behaviour of energy levels as shown in Figs. 2 (a,c) of the main text and in Figs. S5(c,d), where the energy difference between the peaks is plotted as a function of detuning. The linewidths of the corresponding spectral lines extracted from the Lorentzian fit in Fig. S5 and plotted as a function of Δ in Fig2 (b,d) of the main text show the opposite behaviour, as expected for a non-Hermitian spectral degeneracy.

IV. EXPERIMENTAL PARAMETERS VS VARIATION OF DETUNING

The parameters appearing in the generalised complex Gross-Pitaevskii equation (1) of the paper can be calculated according to the change of detuning Δ, or equivalently, the Hopfield coefficient $|X|^2$: $|X|^2 = (1/2)\left[1 + \Delta/\sqrt{\Delta^2 + E_R^2}\right]$,

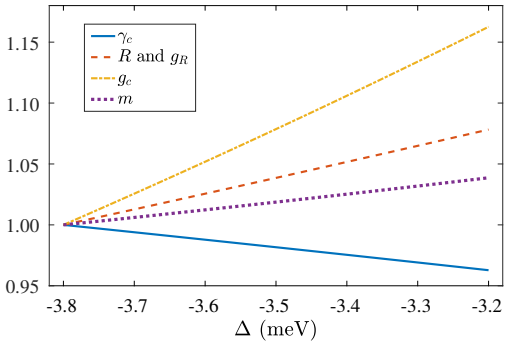

FIG. S6: The change of the system parameters with detuning relative to their base values at $\Delta = -3.8$ meV. Shown are: effective mass m and stimulated scattering rate R, polariton-polariton linear interaction stregth g_c, polariton-reservoir interaction strength g_R, and polariton decay rate γ_c. Rabi splitting is 10 meV.

where E_R is the Rabi splitting at zero detuning. This coefficient characterises the excitonic fraction of the exciton polariton, and therefore affects the effective mass $m \approx m_{ph}/(1-|X|^2)$, the interaction strengths $g_R = |X|^2 g_{ex}$, $g_c = |X|^4 g_{ex}$, and the decay rates $\gamma_c \approx (1-|X|^2)\gamma_{ph}$. Here $m_{ph} \ll m_{ex}$ is the effective mass of the cavity photon, $g_{ex} = 6E_{ex}a_B^2$ characterises interactions between quantum well excitons with the binding energy E_{ex} and the Bohr radius a_B [6], γ_{ph} is the decay rate of the cavity photon, and we assume that the stimulated scattering into the condensed state is more efficient for the more excitonic quasiparticles $R = |X|^2 R_0$. The values of these parameters relative to their base values taken at $\Delta = -3.8$ meV are plotted in Fig. S6 as functions of the photon-exciton detuning in the experimentally relevant range.

The relevant experimental parameters are: $E_R = 10$ meV, $m_{ph} = 1 \times 10^{-5} m_e$, where m_e is the electron mass, $E_{ex} = 10$ meV, $a_B = 7 \times 10^{-3}$ μm, $\gamma_{ph} = 1/120$ ps^{-1}, $\gamma_{ex} = 1$ ns^{-1}, and $R_0 = 0.01$ μm^{2}ps^{-1}.

In the theoretical calculation in the main text, the pump is approximated as:

$$P(r,\theta) = \begin{cases} P_0\, e^{-\frac{(r-r_1)^2}{2\sigma_1^2}} & \text{if} \quad \frac{\pi}{2} \leqslant \theta < \frac{3\pi}{2}, \\ P_0\, e^{-\frac{(r-r_2)^2}{2\sigma_2^2}} & \text{if} \quad -\frac{\pi}{2} \leqslant \theta < \frac{\pi}{2}, \end{cases} \tag{1}$$

where $r_1 = 12$ μm, $\sigma_1 = 4.5$ μm, $r_2 = 9.25$ μ m, σ_2 takes the values between 3 and 3.5 μm, and the value of P_0 well above condensation threshold was chosen to reproduce the crossing and the anti-crossing phenomena in our model. The discontinuity at $\theta = \pm\pi/2$ has been smoothed by a convolution with the tanh function.

V. THE DETERMINISTIC CHARGE OF A VORTEX

The deterministic nature of the sign of the vortex charge observed in our experiments is owed to the break of physical chiral symmetry (P-symmetry) in our system. In 2D systems like ours, the P-symmetry corresponds to the mirror reflection, i.e., inversion of one of the coordinates, e.g., $y \to -y$. We find that our system is asymmetric with respect to such transformations. Indeed, the gradient of the exciton-photon detuning due to the cavity wedge, which is oriented at near 45 degrees to the P-symmetric pump profile shown in Fig. S7(a), translates into the weak linear gradient of the potential along this direction, which is sufficient to make the whole system (and its Hamiltonian) P-asymmetric. That is, the mirror image of this configuration shown in Fig. S7(d), inset, cannot be transformed back into the original configuration by subsequent rotation.

To prove that this is indeed the physical reason for the particular sign of the topological charge of the vortex at the exceptional point, we rotate the pump profile by 90 degrees with respect to the original orientation, as shown in Fig. S7(d). Since the direction of the gradient is unchanged, the combined pump-induced and gradient potential approximately correspond to the mirror-reflection (and rotation) of the original configuration, and the whole system

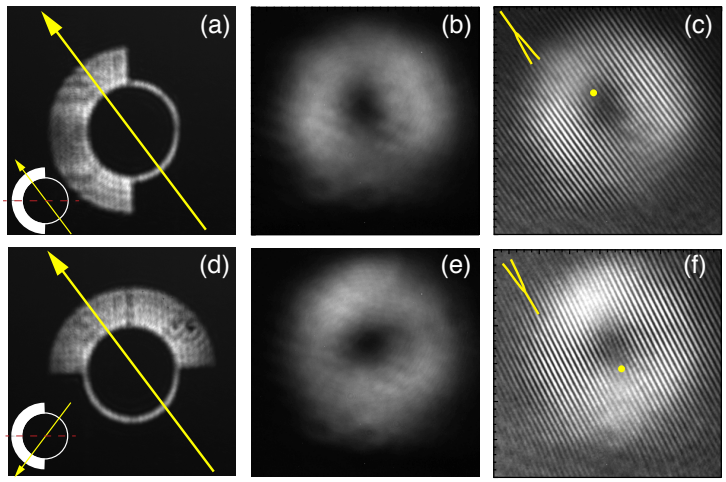

FIG. S7: (a) The relative orientation of the pump and gradient of the cavity wedge and (d) the (nearly) mirror-reflected configuration. The ideal cases are shown in the insets, but due to limitations of the DMD mirror setup, it is difficult to achieve precise mirror-reflected configuration in the experiment. Because the two configurations are not equivalent, they produce either a vortex (b,c) or anti-vortex (e,f) near an exceptional point. The insets in (c,f) show the respective orientation of the forks in the interference fringes, dots mark positions of the forks. The field of view is (a,d) 53×53 μm, and (b,e,c,f) 17.7×17.7 μm.

acquires the opposite chirality. Most importantly, the mode at the exceptional point also swaps its chirality and acquires topological charge of an opposite sign, as seen in S7(c,f). This proves that the physical chirality (P-asymmetry) of the system is indeed responsible for the chosen chirality of the mode at the exceptional point.

VI. THE COUPLED-MODE THEORY

The phenomenological couple-mode model that governs the dynamics of populations of two modes with the principal quantum numbers n and n' near the degeneracy can be written as follows:

$$i\frac{\partial \psi_{n,n'}}{\partial t} = \left[-\nabla^2 + V'(\mathbf{r}) + iV''(\mathbf{r})\right]\psi_{n,n'} + \Omega\,\psi_{n',n}. \tag{2}$$

Here the model is written in the dimensionless form, and the last term represents the coupling (Rabi oscillations) between the states ψ_n and $\psi_{n'}$.

Separating the temporal and spatial dependence of the mode $\psi_n = a_n(t)\varphi_n(\mathbf{r})$, substituting this ansatz into Eq. (2), and integrating out the spatial degrees of freedom, leads to the effective two-mode interaction Hamiltonian in the main text:

$$\hat{H} = \begin{bmatrix} \tilde{E}_n & q \\ q^* & \tilde{E}_{n'} \end{bmatrix}, \qquad \tilde{E}_{n,n'} = E_{n,n'} - i\Gamma_{n,n'}, \tag{3}$$

where $\tilde{E}_{n,n'}$ are the complex eigenenergies of the uncoupled modes and q characterises their coupling strength. The real parts of the eigenenergies away from the spectral degeneracy correspond to the eigenstates $\phi_{n,n'}$ of the effective potential $V'(\mathbf{r})$, the imaginary part is determined by the spatial overlap between the modes and the gain region $\Gamma_{n,n'} \propto N^{-1}\int V''(\mathbf{r})|\phi_n|^2 d^2\mathbf{r}$ and the off-diagonal matrix element is governed by the degree of spatial overlap between the two modes $q \propto N^{-1}\Omega\int \phi_n^*(\mathbf{r})\phi_{n'}(\mathbf{r})\mathrm{d}^2\mathbf{r}$, where $N = \int |u_n(\mathbf{r})|^2 d^2\mathbf{r}$.

As shown in the main text, the exceptional point is defined by the condition: $i\delta\tilde{E}_{EP} = \pm|q|$, where $\delta\tilde{E} = (\tilde{E}_n - \tilde{E}_{n'})/2 \equiv \delta E - i\delta\Gamma$. The two experimental parameters of our system that control the approach to an exceptional point are the exciton-photon detuning, Δ, and the width of the pump-induced reservoir, w, as illustrated in Fig. S8. Variation of the two control parameters of the coupled-mode model $(\delta E, \delta\Gamma)$ approximately correspond to the varying parameters (Δ, w). Indeed, as shown above, the detuning affects the heights of both the real and imaginary parts of the potential, V' and V'', and hence both the energy difference between the modes and values of the complex parts of the eigenenergies. As we move away from the spectral degeneracy, increasing Δ corresponds to increasing δE.

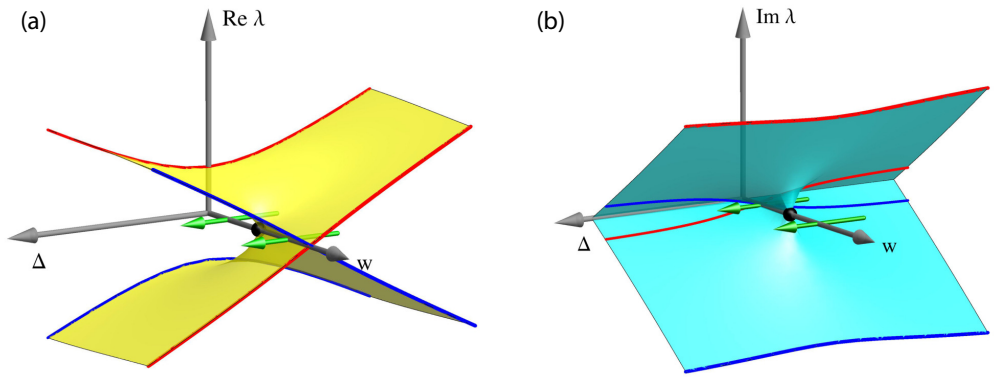

FIG. S8: Schematic plot of the (a) real and (b) imaginary parts of the eigenvalues λ of the effective two-level Hamiltonian $\hat{H}$ near the exceptional point. Blue and red lines show the crossing and anti-crossing between the real and imaginary parts of the eigenvalues. Green arrows indicate the change of parameter Δ in the experiment corresponding to Fig. 2(a,b) and 2(c,d) in the main text.

However, the width of the pump region, w, has a much stronger effect on the gain/loss profile $V''(\mathbf{r})$. Indeed, different polariton modes have different spatial overlaps with the gain region $V''(\mathbf{r})$, and, therefore, the parameter w strongly affects the integral (spatially-averaged) dissipation parameters $\Gamma_{n,n'}$. In the case of the two dipole modes, growing w (with a fixed W) reduces asymmetry of the ring resonator and therefore corresponds to decreasing $\delta\Gamma$.

The chiral mode in Fig. 3(e,f) of the main text is observed as the parameter w is varied along the w-axis in Figs. S8 (a,b), and therefore the real parts of the eigenenergy undergo transition from crossing (at $w = w_2$) to anti-crossing (at $w = w_1 < w_2$). In the experiment, the range of Δ is small and therefore the energy levels in Fig. 2(c) of the main text are nearly parallel, however the corresponding energy difference showin in Fig. S5(d) clearly demonstrates the anti-crossing.

VII. NUMERICAL MODELING

In this section we consider the numerical modelling of the full generalised complex Gross-Pitaevskii equation. The main purpose of this calculation is to confirm that the two different dipole modes, or their linear superposition, are the quasi-steady-states of the system, and therefore can be occupied by polaritons upon condensation in the effective trap. Let us recall that, under continuous wave excitation, the steady state of the system occurs when the reservoir density is [Eq. (2) of the main text]:

$$n_R(\mathbf{r}) = \frac{P(\mathbf{r})}{\gamma_R + R|\psi(\mathbf{r})|^2}. \tag{4}$$

In the limit $\gamma_R \gg R|\psi|^2$, one can approximate $n_R(\mathbf{r}) \approx (P/\gamma_R)\left(1 - R|\psi(\mathbf{r})|^2/\gamma_R\right)$. Defining the new parameters $g = g_R/\gamma_R$, $r = R/\gamma_R$, and $\alpha_{NL} = R^2/\gamma_R$, the Gross-Pitaevskii equation becomes:

$$i\hbar\frac{\partial\psi(\mathbf{r})}{\partial t} = \left\{-\frac{\hbar^2}{2m}\nabla^2 + g_c|\psi(\mathbf{r})|^2 + gP(\mathbf{r}) + \frac{i\hbar}{2}\left[rP(\mathbf{r}) - \gamma_c - \alpha_{NL}|\psi(\mathbf{r})|^2\right]\right\}\psi(\mathbf{r}) \tag{5}$$

This equation, known as the complex Ginzburg-Landau equation [8], holds for a rapidly responding reservoir and is often considered directly for modelling of microcavity polariton field distributions. However, for our case it requires further modification. The ring-shaped pumping distribution introduces an effective trapping potential via the term $gP(\mathbf{r})$, which allows the formation of a discrete set of modes in the system. One expects that the mode chosen by the system will be the one of highest gain (see, e.g., Ref. [7]), and indeed for this reason, solution of the above equation typically results in the population of high energy modes, which have the greatest spatial overlap with the pumping $rP(\mathbf{r})$. Our experimental results have shown that the system instead forms in low energy modes, therefore we also need an account of energy relaxation processes.

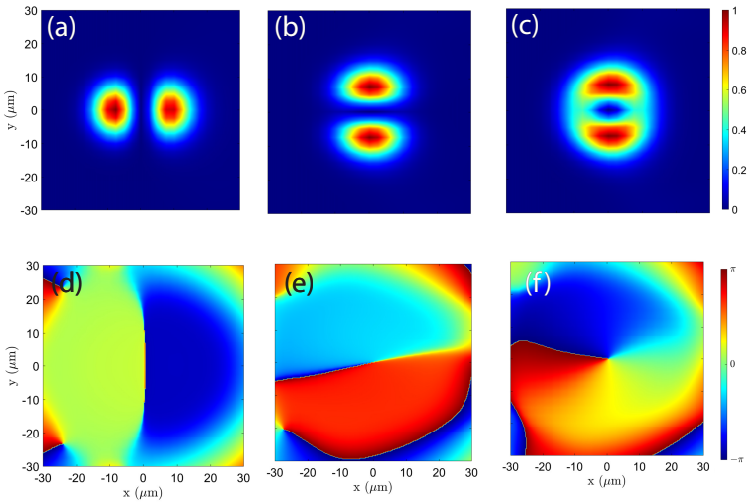

FIG. S9: Numerical solutions of Eq. 5 for different values of r_2. Shown are (a,b,c) probability density distributions and (d,e,f) corresponding phases of the exciton-polariton wavefunctions. Parameters: $\lambda = 2$, $\alpha_{NL} = 1.8\text{meV}\mu\text{m}^2$, $\gamma_c = 1/25\text{ps}^{-1}$, $\epsilon = 1.2$, $\hbar r P_0 = 0.28\text{meV}$, $gP_0 = 2\text{meV}$, $r_1 = 9\mu\text{m}$, $r_3 = 18\mu\text{m}$. m was taken as 10^{-5} of the free electron mass. The width of the Gaussian for smoothing the pump distribution was taken as $3.5\mu\text{m}$; (a) $r_2 = 13\mu\text{m}$, (b) $r_2 = 13.75\mu\text{m}$, (c) $r_2 = 13.55\mu\text{m}$.

Energy relaxation in exciton-polariton systems has been described phenomenologically by the introduction of an additional term into the right-hand side of Eq. 5 [9, 10]:

$$-i\hbar\lambda P(\mathbf{r})\left(-\frac{\hbar^2}{2m}\nabla^2 - \mu(\mathbf{r})\right)\psi(\mathbf{r}) \tag{6}$$

where λ is a parameter determining the strength of energy relaxation and $\mu(\mathbf{r})$ is a local effective chemical potential that should be chosen such that the above term by itself conserves the number of polaritons. The energy relaxation term describes the loss of polaritons with large kinetic energy. To conserve the number of particles, polariton modes with lower kinetic energy, such as the lowest modes in a trap, receive increased gain. More details on how to handle the chemical potential terms are given in Ref. [11].

We considered a pump profile given by:

$$P(\mathbf{r}) = P_0\theta\left(x^2 + (\epsilon y)^2 - r_1^2\right)\left(\theta(x)\,\theta\left(r_2^2 - x^2 - (\epsilon y)^2\right) + \theta(-x)\,\theta\left(r_3^2 - x^2 - (\epsilon y)^2\right)\right) \tag{7}$$

where P_0 is the maximum pump rate, θ denotes the Heaviside step function, r_1 is the pump inner radius, r_2 is the pump outer radius on the left-hand side, and r_3 is the pump outer radius on the right-hand side. We also allowed for an ellipticity of the pump, described by parameter ϵ. The above form of $P(\mathbf{r})$ contains sharp jumps in intensity due to the Heaviside step function. To better represent the experimental configuration, the pump distribution was smoothed by convolution with a Gaussian.

To reproduce the formation of different spatial patterns, we fixed all parameters, except for r_2, which was varied. For simplicity, and to show that the formation of the vortex mode does not require polariton-polariton interactions, we set $g_c = 0$. The result of numerical solution of Eq. 5 (with the modification term 6) is shown in Fig. S9. For varying r_2 we observe the crossover from a horizontal dipole mode (Fig. S9(a) to a vertical dipole mode (Fig. S9(b). The vortex state appears at intermediate values of r_2, as shown in Fig. S9(c).

VIII. HIGHER-ORDER ORBITAL ANGULAR MOMENTUM STATES

In addition to the higher-order orbital momentum state formed in our experiment by hybridisation of two chiral modes, $\psi = \psi_7 + i\,\psi_8 + \psi_9 + i\,\psi_{10}$ (as shown in the main text), Fig. S10 shows a chiral state formed by hybridisation of three modes, $\psi = (\psi_4 + i\,\psi_5) + \psi_6$, with the exceptional point corresponding to ψ_4 and ψ_5. The interferometry image confirms the formation of a double-vortex state with the two resulting vortices having the same topological charge. This double-vortex state can be reproduced by our simple linear theory (see main text), as shown in Fig. S10 (c,d).

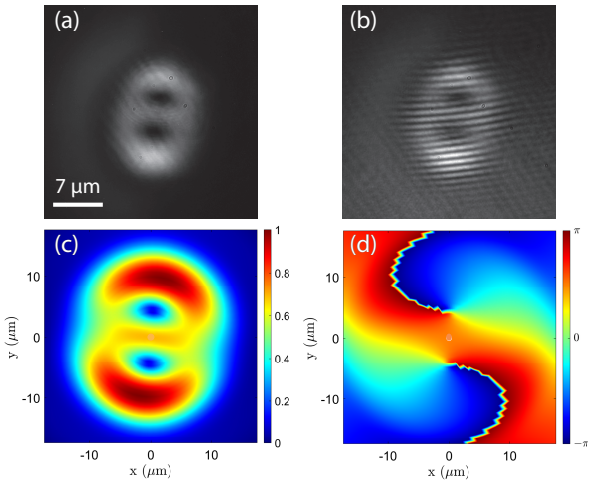

FIG. S10: (a) Experimental real-space photoluminescence image corresponding to the exciton-polariton density in a double-vortex state. (b) Experimental interferometry image of the double-vortex state. (c,d) Theoretically calculated double-vortex state $\psi = (\psi_4 + i\,\psi_5) + \psi_6$, showing the (c) modulus and (d) phase of ψ.

[1] B. Nelsen, G. Liu, M. Steger, D. W. Snoke, R. Balili, K. West, and L. Pfeiffer, Dissipationless Flow and Sharp Threshold of a Polariton Condensate with Long Lifetime, Phys. Rev. X **3**, 041015 (2013).

[2] R. Dall, M. D. Fraser, A. S. Desyatnikov, G. Li, S. Brodbeck, M. Kamp, C. Schneider, S. Höfling, and E. A. Ostrovskaya, Phys. Rev. Lett. **113**, 200404 (2014).

[3] J. Kasprzak, M. Richard, S. Kundermann, A. Baas, P. Jeambrun, J. M. J. Keeling, F. M. Marchetti, M. H. Szymańska, R. André, J. L. Staehli, V. Savona, P. B. Littlewood, B. Deveaud, and Le Si Dang, Nature **443**, 409 (2006); H. Deng, H. Haug, and Y. Yamamoto, Rev. Mod. Phys. **82**, 1489 (2010).

[4] I. V. Basisty, V. Yu. Bazhenov, M. S. Soskin, and M. V. Vasnetsov, Opt. Commun. **103**, 422 (1993).

[5] F. Manni, T. C. H. Liew, K. G. Lagoudakis, C. Ouellet-Plamondon, R. André, V.Savona, and B. Deveaud, Phys.Rev.B.**88**, 201303(R) (2013).

[6] F. Tassone and Y. Yamamoto, Phys. Rev. B **59**, 10830 (1999).

[7] S. Khan and H. E. Türeci, Phys. Rev. A **94**, 053856 (2016)

[8] J. Keeling and N. G. Berloff, Phys. Rev. Lett. **100**, 250401(2008).

[9] M. Wouters, New J. Phys., **14**, 075020 (2012).

[10] M. Wouters, T. C. H. Liew, and V. Savona, Phys. Rev. B, **82**, 245315 (2010).

[11] C. Antón, T. C. H. Liew, G. Tosi, M. D. Martín, T. Gao, Z. Hatzopoulos, P. S. Eldridge, P. G. Savvidis, and L. Viña, Phys. Rev. B, **88**, 035313 (2013).